Experimental demonstration of superresolution of partially coherent light sources using parity sorting

S. A. Wadood,[1,2] **Kevin Liang,**[1,2] **Yiyu Zhou,**[1,2] **Jing Yang,**[2,3] **M. A. Alonso,**[1,2,4] **X.-F. Qian,**[5] **T. Malhotra,**[2,3,6] **S. M. Hashemi Rafsanjani,**[7] **Andrew N. Jordan,**[2,3,8] **Robert W. Boyd,**[1,2,3,9] **and A. Nick Vamivakas**[1,2,3,10,*]

[1]*The Institute of Optics, University of Rochester, Rochester, New York 14627, USA*

[2]*Center for Coherence and Quantum Optics, University of Rochester, Rochester, New York 14627, USA*

[3]*Department of Physics and Astronomy, University of Rochester, Rochester, New York 14627, USA*

[4]*Aix Marseille Univ, CNRS, Centrale Marseille, Institut Fresnel, UMR 7249, 13397 Marseille Cedex 20, France*

[5]*Department of Physics and Center for Quantum Science and Engineering, Stevens Institute of Technology, Hoboken, NJ 07030, USA*

[6]*Currently with Facebook Reality Labs, Redmond, WA, USA*

[7]*Department of Physics, University of Miami, Coral Gables, Florida 33146, USA*

[8]*Institute for Quantum Studies, Chapman University, Orange, California 92866, USA*

[9]*Department of Physics, University of Ottawa, Ottawa, Ontario K1N 6N5, Canada*

[10]*Materials Science, University of Rochester, Rochester, NY 14627, USA*

[*]*nick.vamivakas@rochester.edu*

Abstract: Analyses based on quantum metrology have shown that the ability to localize the positions of two incoherent point sources can be significantly enhanced over direct imaging through the use of mode sorting. Here we theoretically and experimentally investigate the effect of partial coherence on the sub-diffraction limit localization of two sources based on parity sorting. With the prior information of a negative and real-valued degree of coherence, higher Fisher information is obtained than that for the incoherent case. Our results pave the way to clarifying the role of coherence in quantum-limited metrology.

1. Introduction

The resolution of imaging systems is limited by the size of the diffraction-limited point spread function (PSF) [1]. To quantify this resolution, the Rayleigh criterion has been proposed and widely used [2]. Recently, the analysis of optical resolution has been recast in terms of Fisher Information (FI) [3–5], which quantifies the precision of measurements and is inversely proportional to the parameter estimation error. Generally, the FI of the estimation of separation δ between two spatially incoherent point sources depends on the type of measurement performed on the image plane field. In the case of direct detection of image plane intensity, the FI goes to zero as $\delta \to 0$, an effect termed as Rayleigh's curse. In their seminal work [3], Tsang et al. showed that Rayleigh's curse can be overcome if the optical field is detected by an appropriate spatial mode demultiplexer (SPADE), given prior knowledge of two equally bright and incoherent point sources versus a single emitter. It has been verified experimentally, as a demonstration of superresolution over direct imaging, that the FI for such a scheme is constant as $\delta \to 0$ [6–10].

The sources, however, can have a non-zero coherence between them [11]. In fact, spatial coherence is a key parameter affecting the resolution of imaging systems [12]; coherent illumination techniques can offer enhanced resolution in microscopy [13] and two-point direct imaging [14,15]. Moreover, coherence imaging can offer significant practical advantages over

conventional direct imaging systems, for example in the very long baseline radio interferometry (VLBI) used for black hole imaging [16]. It is then natural to ask how spatial coherence between the two sources affects the resolution obtained by SPADE. Recent theoretical works have extended the scope of the two-point estimation problem to include the general case of partial coherence among the two sources [17–22]. In particular, it was shown that Rayleigh's curse can still be avoided for a known degree of spatial coherence γ [18,19,22]. For the case of $\gamma<0$, an even greater sensitivity for SPADE was predicted than the incoherent case. The increased sensitivity needs to be carefully interpreted, taking into account photon budgeting considerations [21]. Experimental demonstration of SPADE with partial coherence, however, has been lacking. The main result of our work is to experimentally demonstrate the breaking of Rayleigh's curse for partially coherent light sources using SPADE. In doing so, we also distill and connect the different elements of previous theoretical works.

In Section 2, we derive the classical FI of our experimental setup for partially coherent fields. Special attention is paid to a priori assumptions and how they affect the obtained FI. The connection between previous works is also made clear in this section. Section 3 explains the experimental setup, the generation of spatial coherence, and a discussion of estimation statistics. Section 4 summarizes the results.

2. Theory

In this section we outline the calculation of the classical FI for parity sorting of partially coherent fields. Note that parity sorting falls under the scheme of binary SPADE (BSPADE), which is a family of measurements that simplifies SPADE at the cost of losing large-delta information [3,23]. For the sub-Rayleigh regime, it has been shown that a measurement of the even and odd projections of the input field has an FI that converges to the quantum optimal FI [7,9]. Here we show explicitly how different a priori assumptions yield different FI curves. The physical problem is the following: Two point sources separated by δ and having a degree of spatial coherence γ are imaged by an imaging system with a finite-sized aperture and a characteristic PSF width σ. The goal is to perform quantum-limited estimation of δ in the sub-Rayleigh regime ($\delta<\sigma$) by performing parity sorting on the image plane field.

A partially coherent field is described by its cross-spectral density (CSD) function $W(x_1, x_2)$ [11]. To proceed, we first note that W can be decomposed via the coherent mode decomposition (CMD) [24]. For our problem, the simplest choice of modes is to decompose W in the symmetric (in phase) and antisymmetric (out of phase) combinations of the two sources. In the image plane, $W(x_1, x_2)$ is given as

$$W(x_1, x_2) = N_0 \kappa \sum_{k=1}^{2} p_k \phi_k^*(x_1)\phi_k(x_2), \tag{1}$$

where N_0 is the average object plane photon number *emitted* by each point source, κ is a space-invariant efficiency factor dictated by the aperture loss, $\phi_k(x) = f_+(x) - e^{ik\pi}f_-(x)$ are the symmetric ($k = 1$) and antisymmetric ($k = 2$) coherent modes, $f_\pm(x) = f(x \pm \delta/2)$ are the two point spread functions separated by δ - the parameter to be estimated, p_k is a real number such that $0 \le p_k \le 1$, and $p_1 + p_2 = 1$. In what follows, the terms even and odd modes are used interchangeably with symmetric and antisymmetric modes. We assume Gaussian PSFs of width σ such that $f(x) = \frac{e^{-x^2/4\sigma^2}}{(2\pi\sigma^2)^{1/4}}$ is the field PSF. The total number of photons in the image plane is given by

$$N_t = \int dx W(x, x) = 2N_0\kappa(1 + \gamma d), \tag{2}$$

where $d = \int dx f_+(x)f_-(x) = e^{-\delta^2/(8\sigma^2)}$ is the overlap integral of the two shifted PSFs, and $\gamma = p_1 - p_2$ is an effective degree of spatial coherence between the two sources. It is here that

we first encounter the departure from the incoherent estimation problem; for $\gamma \neq 0$, N_t depends on the parameter δ to be estimated. Hence, it is necessary to spend some time clarifying the interpretation of the FI for partially coherent sources. For a parity sorter, the photon numbers in the even and odd ports are, respectively,

$$N_1 = N_0 \kappa p_1 \int dx |\phi_1(x)|^2 = N_0 \kappa (1 + \gamma)(1 + d)$$

$$N_2 = N_0 \kappa p_2 \int dx |\phi_2(x)|^2 = N_0 \kappa (1 - \gamma)(1 - d). \tag{3}$$

Equations (2) and (3) are derived in Supplement 1, Section S1. We assume that γ, κ are known a priori. If we know N_0 and the only unknown in the experiment is δ, then assuming Poisson statistics it can be shown [3] that the FI for parity sorting is given by

$$\frac{F_\delta(\delta, \gamma)}{2N_0\kappa} = \frac{\delta^2 d^2}{16\sigma^4} \left(\frac{1 - \gamma d}{1 - d^2} \right), \tag{4}$$

where the subscript δ denotes that δ is the unknown parameter. Note that $F_\delta(\delta, \gamma)$ is normalized by $2N_0\kappa$, the total object plane photons multiplied by the loss factor. $F_\delta(\delta, \gamma)$ is plotted in Fig. 1(a), and κ has been absorbed into N_0 for the plot. These curves show that the highest FI is achieved for $\gamma = -1$. The physical operation of parity sorting affords some intuition about this FI behavior. For $\gamma = -1$, all photons are routed to the odd port, and we have $N_1 = 0$ and $N_2 = 2N_0\kappa(1 - d)$. Knowing the total emitted photon number $2N_0$ and the total detected photon number N_2 allows us to estimate δ directly. For $\delta \ll \sigma$, the power in the odd port is well approximated as $N_0\kappa(1 - \gamma)\delta^2/8\sigma^2$. Thus for sub-Rayleigh separations, the odd port has the most photons for $\gamma = -1$, and hence the highest FI.
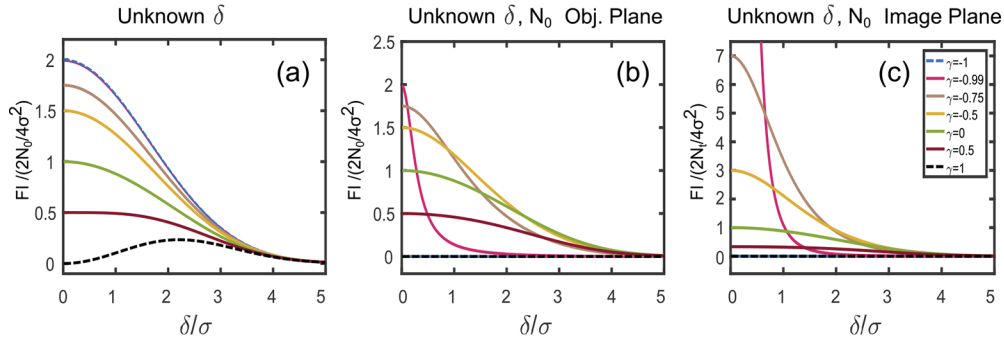

Fig. 1. Expected FI for the parity sorter plotted versus δ/σ. A higher FI corresponds to a lower estimation error. a: FI prediction for the case when δ is the only unknown parameter. For this case, $\gamma = -1$ gives the highest FI (dashed blue line on top of the $\gamma = -0.99$ curve), as predicted by the Tsang–Nair model [18]. b: FI prediction for the case of unknown input photon number N_0. For this case, the FI is zero for $|\gamma| = 1$. As $\gamma \to -1$, the FI curve gets concentrated near $\delta = 0$, but is still bounded above by twice the FI for $\gamma = 0$. The curves in (a,b) are normalized by the object plane photon numbers. c: FI prediction normalized by the image plane photon number for the case of unknown N_0. These curves are related to the curves in (b) by the weight factor of $(1 + \gamma d)$ as explained in the text. As $\gamma \to -1$, this image plane FI diverges and gets concentrated around $\delta = 0$, a result which was predicted using a quantum calculation in [19,21]. As explained in the text, the information conveyed by curves (b,c) is the same. Note that the $\gamma = 0$ curves (green line) are same in all the figures.

It is not uncommon, however, that an experimentalist only has access to image plane photons, and does not have knowledge of N_0. When both δ and N_0 are unknown, the FI is found from the

multiparameter Cramer–Rao bound (CRB); this FI is given by

$$\frac{F_{\delta,N_0}(\delta,\gamma)}{2N_0\kappa} = \frac{\delta^2 d^2}{16\sigma^4(1+\gamma d)}\left(\frac{1-\gamma^2}{1-d^2}\right),\tag{5}$$

and is plotted in Fig. 1(b). Note that as $\gamma \rightarrow -1$, $F_{\delta,N_0}(\delta,\gamma)$ becomes concentrated near $\delta = 0$. While Rayleigh's curse is avoided for $\gamma < 0$, i.e., $\lim_{\delta\rightarrow 0} F_{\delta,N_0}(\delta,\gamma)/2N_0\kappa = (1-\gamma)/4\sigma^2$, the FI is effectively zero for all $\delta \neq 0$ and $\gamma = -1$. Figures 1(a,b) clearly show how the knowledge or ignorance of the object plane photon number affects the FI for δ estimation in the presence of partial coherence. A derivation of Eqs. (4) and (5) is presented in Supplement 1, Section S2.

We can now ask the more practical question of how to estimate δ when we only detect the image plane field, and have no knowledge of N_0 ? In this case one can use the normalized modal weights $m_{1,2} = N_{1,2}/N_t$ which are *independent of N_0*. The statistics are described in this case by a binomial likelihood function [25]. We can then calculate the *image plane* FI by the formula

$$\begin{aligned}F_{img}(\delta,\gamma) &= \sum_{k=1,2}\frac{1}{m_k(\delta,\gamma)}\left(\frac{\partial m_k(\delta,\gamma)}{\partial\delta}\right)^2\\ &= \frac{\delta^2 d^2}{16\sigma^4(1+\gamma d)^2}\left(\frac{1-\gamma^2}{1-d^2}\right),\end{aligned}\tag{6}$$

where the subscript 'img' denotes image plane and the function is plotted in Fig. 1(c). We emphasize that F_{img} is normalized per image plane photon; physically, Eq. (6) quantifies the information provided by a single photon in the image plane, and is agnostic to the number of object plane photons. Figure 1(c) then shows that given equal number of photons in the image plane, $\gamma < 0$ can offer increased sensitivity in the regions $\delta \ll \sigma$. Note that Eq. (6) is related to Eq. (5) by a simple 'weight' factor of $(1 + \gamma d)$, which also relates the image and object plane photon number in Eq. (2). While the image plane FI might increase for $\gamma < 0$, more object plane photons are needed to maintain a constant image plane photon number, a 'cost' that is captured by the factor of $(1 + \gamma d)$. The image plane FI is also zero for $\gamma = -1$, in which case all clicks occur at the odd port for all δ. If the experimentalist does not know N_0, they do not get any information about δ from just measuring clicks at the odd port. In any case, Figs. 1(b) and 1(c) give the same information, as there is a one-to-one correspondence between the two curves. Alternatively, the lower bound on the variance of an unbiased estimator can equivalently be found from either Eq. (5) or Eq. (6). As a specific example, suppose we have $2N_0\kappa = 100$, and $(1 + \gamma d) = 0.1$ for a specific δ and γ, which means that we have 10 photons in the image plane. Then the lower bound on the variance of an unbiased estimator $\hat{\delta}$ satisfies $\mathrm{Var}[\hat{\delta}] \geq 1/(10 F_{img}) = 1/(100 F_{\delta,N_0})$, where $F_{\delta,N_0} = (1 + \gamma d)F_{img}$.

Incidentally, the aforementioned discussion provides clarity to the debate between, among others, the Tsang–Nair (TN) model [18] and the Larson–Saleh (LS) model [19]. Strictly speaking, the TN model assumes knowledge of N_0, while the LS model assumes an unknown N_0. Specifically, Fig. 1(a) agrees with the TN model, and Fig. 1(c) agrees with the LS model. Figure 1(b) bridges the TN and LS models. We note that Hradil et. al. [21] also advocated the use of the weighted version of image plane FI to take into account the image plane photon number variation with γ, δ, and their results also imply the curves in Fig. 1(b). Depending on the a priori assumptions afforded by the experimental setup, either TN or LS models will correctly describe the estimation statistics. Note that a similar observation has been made for coherent microscopy [26], which advocates the 'mandatory inclusion of information about underlying *a priori* assumptions' when discussing resolution claims.

We mention that the parity sorter achieves a quantum limited performance. To see this, note that our classical FI calculations coincide with the predictions of the quantum FI in [19,21] for a

known δ, γ and unknown N_0. The notion of a quantum FI for a known N_0 is still being actively explored [27], and is beyond the scope of this work.

Having clarified the issue of the FI interpretation for partial coherence, we can now proceed to discuss the experiment. Realistically, we will use the image plane model as it reflects a common situation in imaging, microscopy, and astronomy. Note that realistic situations have more than just δ and N_0 as possible unknowns. For example, our analysis till now has assumed the presence of only two sources, equal intensities of the two sources, a known centroid of the objects to which the parity sorter is aligned, and, most importantly, a known γ. In practice, one needs a combination of direct imaging, coherence interferometry, and parity sorting to estimate these unknown parameters. The application of quantum metrology-inspired ideas such as SPADE to practical situations is an active field of research [28–31]. These considerations, however, are not relevant to our proof-of-principle experiment in which we consider only δ and N_0 as the unknown parameters.

3. Experiment

3.1. Generation of partial coherence

We use a parity sorter to perform SPADE on two spatially partially coherent sources. To generate partial coherence, we use the CMD [24]. Physically, such a CMD means that the spatial coherence at the input plane to the SPADE setup can be engineered by incoherently mixing appropriately scaled symmetric and antisymmetric modes. This can be realized by adding a path difference between coherent modes that is larger than the laser coherence length. Alternatively, we can 'switch' between the modes in time, with the switching time longer than the laser coherence time, and add the recorded intensities digitally [32,33]. The CMD therefore allows us to generate spatial coherence 'offline', by performing the intensity summation electronically. To generate an intensity distribution corresponding to a specific γ in Eqs. (3), we can post-select from a set of recorded intensities of $\phi_{1,2}$ modes. This allows a great simplification of the experiment with respect to the precise control of γ. Nevertheless, the CMD technique has a physical drawback; we are not looking at two real point sources, but at the image plane field generated *as if* the point sources with a given δ and γ were actually present. Due to this characteristic of CMD, we cannot access the object plane curves of Figs. 1(a) and 1(b), as is also explained at the end of Section 3.3.

Figure 2(a) shows the coherent mode generation portion of the setup, which contains an SLM and a $4f$ spatial filter. The coherent modes for a particular δ are generated via a phase grating implemented on a spatial light modulator (SLM). The SLM can be used to generate a field $\psi(x, y)$ with an arbitrary transverse amplitude and phase profile. To that end, we implement a phase grating $\exp[i(\Pi(x, y))]$ on the SLM. The grating is constrained such that the first-order term in its Fourier expansion equals $\psi(x, y) = \phi_k(x)f(y)$, where $\phi_k(x)$ is the kth coherent mode and $f(y)$ is the Gaussian PSF defined after Eq. (1). We add a linear phase grating and use a $4f$ spatial filter to isolate the first diffraction order, which is proportional to $\psi(x, y)$. The details on the algorithm to 'encode' the field into the phase grating are given in [34]. Note that there are limits set on the spatial frequency content of the beams that can be generated. These limits are dictated primarily by the pixel pitch of the SLM, and the range of phase modulation that the liquid crystals can impart. The SLM model used in our experiment is HAMAMATSU X10468-02, which has a pixel pitch of $20\mu m$ and a phase modulation range of 2π. Due to the small pixel pitch, any discretization effects are negligible in our experiment. The SLM only responds to a horizontally polarized beam (polarization axis parallel to the optical table). The inset in Fig. 2(a) shows the phase grating implemented on the SLM to generate the coherent modes. The high spatial frequency fringes show the linear grating implemented to separate the desired mode on the first diffraction order. Note that the phase mask is qualitatively very similar to the beam itself. The beam is relayed to the parity sorter, shown in Fig. 2(b), with $4f$ systems. The symmetric or antisymmetric modes generated via the SLM have $\sigma = 327 \pm 4\mu m$. Note that we are not

changing the temporal coherence properties; all the beams used are quasimonochromatic and therefore temporally coherent.
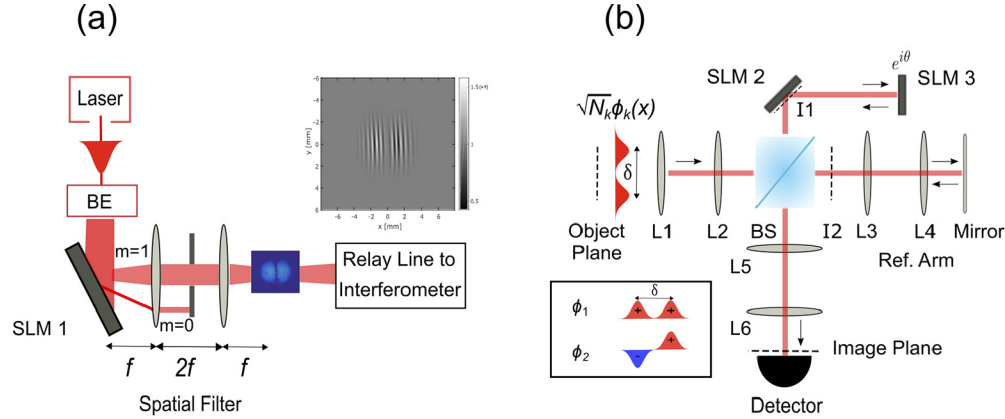

Fig. 2. a: Generation of Coherent Modes: A 795 nm linearly polarized Gaussian beam passes through a beam expander (BE) and is then transformed into either a symmetric (ϕ_1) or antisymmetric (ϕ_2) mode via a mode converter consisting of a phase SLM and a spatial filtering setup, which selects the $m = 1$ diffraction order. The beam is relayed to the interferometer with $4f$ systems. The mode amplitudes are set to $\sqrt{N_k} = \sqrt{N_t m_k}$, with m_k being the normalized modal weights and N_t being an arbitrary image plane photon number, to generate the CSD given by Eq. (1). Polarization optics and attenuators, not shown in the figure, are used to control the power of the beam. Inset shows the phase mask implemented on the SLM to generate the antisymmetric mode with $\delta/\sigma = 0.2$. The high spatial frequency tilt fringes form the grating that routes the desired mode into the first diffraction order. b: Parity sorter, a Michelson type image inversion interferometer which separates the even and odd components of the input field. In one arm, the two SLMs form a $2f$ system with SLM 2 having a focal length of 600 mm , SLM 3 having a focal length of 300 mm, and the distance between the two SLMs equal to 600 mm. This arm implements the transformation $(x, y) \rightarrow (-x, -y)$. The input $4f$ relays the beam from the coherent mode generation part of the setup with unit magnification ($f_{L1}, f_{L2} = 200$ mm). The $4f$ in the reference arm has a magnification of 0.5 ($f_{L3} = 200$ mm, $f_{L2} = 100$ mm) (double pass magnification is unity). The final $4f$ system in the output arm relays to the detector the field at SLM 2 and the reference arm field with a 0.5 magnification factor ($f_{L5} = 200$ mm, $f_{L6} = 100$ mm). The power in the even and odd modes can be measured by setting the phase difference θ, implemented on SLM 3, to 0 and π respectively. In the experiment, all modes used are symmetric about the y axis such that $E(x, -y) = E(x, y)$. The interferometer then works as a parity sorter in the *x*-direction. $I1, I2$ denote the intermediate image planes in the SLM and reference arms respectively. BS: Beamsplitter, Ref. arm: Reference arm.

3.2. SPADE using parity sorting

After generating partially coherent fields, the next step is to perform parity sorting on the field described by Eq. (1). The beam flux can be adjusted using polarization optics. The parity sorter consists of a Michelson type image inversion interferometer that sorts the input field based on its parity, as shown in Fig. 2(b). Figure 2(b) shows the top arm having 2 SLMs separated by a distance of 600mm. SLM 2 has a focal length of 600 mm and SLM 3 a focal length of 300 mm. The optical power on SLM 2 cancels the quadratic phase at the image plane of SLM 3, which coincides with the SLM 2 plane. The top arm is then effectively equivalent to a $2f$ imaging system, with an extra quadratic phase to cancel the defocus due to diffraction, and implements the transformation $(x) \rightarrow (-x)$. The reference arm with the $4f$ system images the field with unity

magnification, after two reflections. The global phase difference θ between the two arms for the signal beam is also implemented on SLM 3. Experimental details of the interferometer are described in Ref. [35] (For parity sorting, we set $\alpha = \pi$ in Eqs. (1–3) of Ref. [35]). The field at the output of the interferometer is

$$E_{out}(x) = \frac{\sqrt{N_k}}{2}(\phi_k(x) + e^{i\theta}\phi_k(-x)), \tag{7}$$

where $k = 1, 2$, and N_k is the photon number in the input mode ϕ_k. We remind the reader that ϕ_k is spatially coherent in Eq. (7). Note that the coherent modes used are symmetric in y, so the 1D analysis is valid for the experiment. The interferometer is path stabilized using a PID loop connected to a piezo on the reference arm mirror. To monitor the phase fluctuations for the PID loop, a separate vertically polarized beam (not shown in Fig. 2(b)) is sent to the interferometer, separated before the detector via a polarizing beam splitter, and its measured power is fed to the PID loop. Note that the SLMs do not respond to the vertically polarized beam.

To project onto the even and odd components of the field, we can choose $\theta = 0, \pi$ in Eq. (7). As explained in Section 3.1, we send only one of the coherent modes ϕ_k at a given time. To generate CSD for a given γ, we add the measured intensities offline. Details of the offline coherence generation are given in Supplement 1, Section S3. For $\theta = 0(\pi)$, all of the symmetric (antisymmetric) mode power will be directed to the detector, while the antisymmetric (symmetric) mode will destructively interfere at the detector. For $\theta = 0(\pi)$ the output is called as the even (odd) port.

3.3. Estimation Statistics

The goal of superresolution is to estimate δ for regions of $\delta < \sigma$. To estimate δ, we use maximum likelihood estimation (MLE) on the measured normalized modal weights $m_{1,2}$. Sample measurements of the modal weights are shown in Supplement 1, Section S3. Because we normalize the modal weights by the image plane photons, we use a binomial likelihood function for the parity sorter [25]. The estimated $\hat{\delta}$ is shown in Fig. 3(a). Note that all the estimated δ's are below the Rayleigh limit ($\delta = \sigma$), which demonstrates the ability of the parity sorter to perform superresolution. For δ in the interval $[0.2, 1]\sigma$ (in increments of 0.1σ), we take 100 images each of the symmetric and antisymmetric modes, thus getting 100 ML estimates and the corresponding variance. We have not observed any bias in the estimates, as evident in Fig. 3(a), where the mean of the estimates are equal to the true value of δ/σ. The variance in the MLE estimates, which is related to the inverse of the FI, is too small to be noticed in Fig. 3(a). Nevertheless, the variance of an unbiased estimator is lowerbound by the Cramer–Rao bound (CRB), which is related to the inverse of the FI. Formally, $\text{Var}[\hat{\delta}] \geq (N_t F_{img})^{-1}$, where $\text{Var}[\hat{\delta}]$ is the variance in the MLE estimator $\hat{\delta}$, and F_{img} is the image plane FI as given by Eq. (6) and shown in Fig. 1(c). Figure 3(b) shows the normalized Mean Square Error (MSE) $= N_t\text{Var}[\hat{\delta}]$ as a function of δ and two values of $\gamma = 0, -0.75$. More importantly, Fig. 3(b) shows that the MSE for $\gamma = -0.75$ is *below* the CRB for the $\gamma = 0$ case. In other words, not only is Rayleigh's curse avoided for $\gamma = -0.75$, the estimation is more precise than the incoherent case of $\gamma = 0$. Note that the MSE are still offset from the CRB. To truly saturate the CRB, the system must be shot noise limited, and any other noise source will raise the MSE. Apart from shot noise, another source of noise in our system are the phase fluctuations in the interferometer when it is biased at $\theta = 0$ or π (See Fig. 2(b)). Furthermore, the MSE for $\gamma = 0, -0.75$ might appear correlated, for example at $\delta = 0.2, 0.3$. This is because the same set of images are used for CMD of both $\gamma = 0, -0.75$, and hence both $\gamma = 0, -0.75$ MSE's will be affected by the same phase fluctuations; if the $\gamma = 0$ MSE is higher, so will be the $\gamma = -0.75$ MSE. Finally, the CRB curves in Fig. 3(b) are nearly equivalent to the quantum CRB predicted for $\delta < \sigma$ [19], and therefore our measurements represent near quantum-limited localization of partially coherent sources [36].
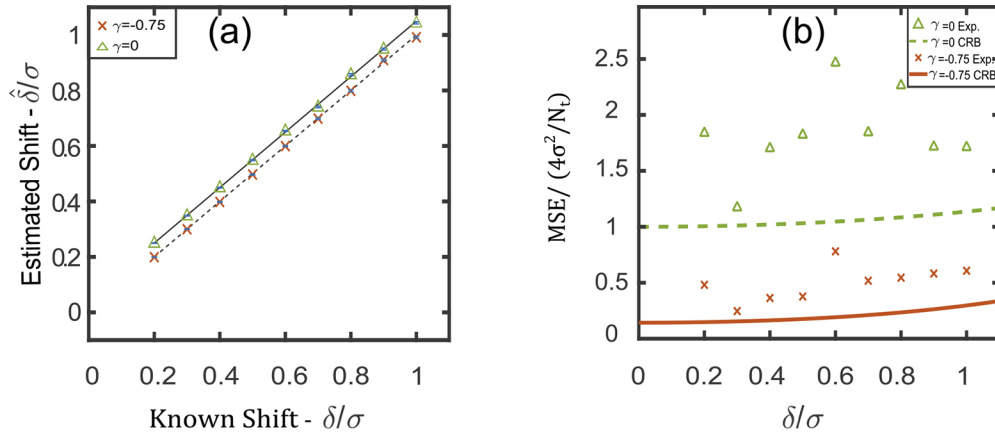
Fig. 3. a: Estimated shift $\hat{\delta}/\sigma$ for $\gamma = 0, -0.75$ using MLE on the measured modal weights. The estimated shifts are all below the Rayleigh limit ($\delta = \sigma$). Each point represents the mean MLE of 100 measurements. The error bars are too small to be noticed on the graph but are still bounded by the CRB, as shown in (b). Note that the $\gamma = 0$ estimates are not biased; to distinguish the two data sets, we introduce a vertical offset between the $\gamma = 0$ and the $\gamma = -0.75$ estimates. Both $\gamma = 0$ and $\gamma = -0.75$ estimates are in good agreement with the expected shifts. b: Measured MSE for $\gamma = 0$ (green triangles) and $\gamma = -0.75$ (red crosses). For each data point, ML estimates from 100 trials were used to calculate the variance. Note that for a given δ/σ, the MSE for $\gamma = -0.75$ is consistently less than the MSE for $\gamma = 0$. The dashed green and solid red lines indicate the CRB for $\gamma = 0, -0.75$ respectively. The CRB is given by the inverse of Eq. (6). Technical noise factors causing the discrepancy between theory and experiment are explained in the main text.

The reader might observe that no statistics for $|\gamma| = 1$ are shown in Fig. 3. As discussed in Section (2), the FI for $|\gamma| = 1$ is zero for all δ if N_0 is unknown. The likelihood function in this case is independent of δ for $|\gamma| = 1$, and hence δ cannot be estimated *in principle*. N_0 is unknown in our experiment because we generate the image plane field directly through unitary transformations and not through a Gaussian aperture that scales the coherent modes according to the $(1 \pm d)$ factor in Eqs. (3). While our system has an effective 'aperture' loss factor that connects the source photon number to the image plane photon number, this loss factor is independent of δ for the coherent modes generated by the SLM, as is also reported in Supplement 1, Section S4. The experiment is the generalization of previous localization experiments on incoherent beams [7,9]. This technique allows 1) a great experimental simplification with regard to avoiding the need to perform precise fabrication of point sources with different separations and 2) to circumvent issues of low photon budget and spurious diffraction effects from the source geometries. However, this technique fails to provide access to an effective object plane photon number which is related to the image plane photon number by the factor of $(1 + \gamma d)$, and hence does not allow us to reconstruct results of Figs. 1(a) and 1(b). Barring these technical difficulties, our theoretical and experimental results are easily generalized to the case of a known N_0. We note that having access to only the image plane photon number is however a common situation in optical physics, where one does not have an independent probe on the object plane photons. Our results are therefore valid for a large variety of microscopy and imaging experiments. The details of image processing and the photon number in Fig. 3 versus δ are given in Supplement 1, Section S4.

4. Conclusion and outlook

We have carried out a theoretical analysis of superresolution of partially coherent light sources using parity sorting. For partially coherent sources, the object plane photon number was identified as a relevant parameter that affects the obtainable FI, and that connects the different results of previous works [18,19,21]. We also performed parity sorting on two Gaussian PSFs with varying degrees of spatial coherence. Our results show that partial anticorrelation of the two sources increases the FI of δ estimation. Therefore, Rayleigh's curse can be avoided for partially coherent sources. The proof-of-principle experiment paves the way to using coherence as a resource in quantum-limited metrology. Our analysis assumes a real, known value of γ. Further studies could include concurrent estimation of δ and γ, for which a vanishing FI with $\delta \to 0$ is predicted [17,22]. The natural extension of the current work is to consider the more realistic case of multiparameter estimation of a complex γ, the centroid and intensity ratio of the two sources [22], and the effects of cross-talk in the SPADE setup [28–30,37]. While we have been primarily concerned with the two-point problem, the technique of SPADE can also tackle the more general problem of imaging an extended object scene. There the problem reduces to estimation of moments of the object in the sub-diffraction limit, a case which was treated for incoherent objects [4,38–40]. It is an open question as to how these theoretical works generalize to the case of partially coherent object distributions.

Disclosures. The authors declare that there are no conflicts of interest related to this article.

Data availability. The raw data for Fig. 3 and Supplement 1 are available from the authors upon request. The data were processed in MATLAB, and the data processing codes are also available from the authors upon request.

Supplemental document. See Supplement 1 for supporting content.

References

1. J. W. Goodman, *Introduction to Fourier Optics* (Roberts and Company Publishers, 2005).
2. L. Rayleigh, "Xxxi. Investigations in optics, with special reference to the spectroscope," Lond. Edinb. Dubl. Phil. Mag. J. Sci. **8**(49), 261–274 (1879).
3. M. Tsang, R. Nair, and X.-M. Lu, "Quantum theory of superresolution for two incoherent optical point sources," Phys. Rev. X **6**(3), 031033 (2016).
4. S. Zhou and L. Jiang, "Modern description of rayleigh's criterion," Phys. Rev. A **99**(1), 013808 (2019).
5. J. Yang, S. Pang, Y. Zhou, and A. N. Jordan, "Optimal measurements for quantum multiparameter estimation with general states," Phys. Rev. A **100**(3), 032104 (2019).
6. M. Paúr, B. Stoklasa, Z. Hradil, L. L. Sánchez-Soto, and J. Rehacek, "Achieving the ultimate optical resolution," Optica **3**(10), 1144–1147 (2016).
7. W.-K. Tham, H. Ferretti, and A. M. Steinberg, "Beating Rayleigh's curse by imaging using phase information," Phys. Rev. Lett. **118**(7), 070801 (2017).
8. F. Yang, A. Tashchilina, E. S. Moiseev, C. Simon, and A. I. Lvovsky, "Far-field linear optical superresolution via heterodyne detection in a higher-order local oscillator mode," Optica **3**(10), 1148–1152 (2016).
9. Z. S. Tang, K. Durak, and A. Ling, "Fault-tolerant and finite-error localization for point emitters within the diffraction limit," Opt. Express **24**(19), 22004–22012 (2016).
10. Y. Zhou, J. Yang, J. D. Hassett, S. M. H. Rafsanjani, M. Mirhosseini, A. N. Vamivakas, A. N. Jordan, Z. Shi, and R. W. Boyd, "Quantum-limited estimation of the axial separation of two incoherent point sources," Optica **6**(5), 534–541 (2019).
11. L. Mandel and E. Wolf, *Optical Coherence and Quantum Optics* (Cambridge University Press, 1995).
12. J. W. Goodman, *Statistical Optics* (John Wiley & Sons, 2015).
13. P. Ferraro, A. Wax, and Z. Zalevsky, *Coherent light microscopy: Imaging and quantitative phase analysis*, vol. 46 (Springer Science & Business Media, 2011).
14. D. N. Grimes and B. J. Thompson, "Two-point resolution with partially coherent light," J. Opt. Soc. Am. **57**(11), 1330–1334 (1967).

15. V. Nayyar and N. Verma, "Two-point resolution of gaussian aperture operating in partially coherent light using various resolution criteria," Appl. Opt. **17**(14), 2176–2180 (1978).

16. The Event Horizon Telescope Collaboration, et al. "First m87 event horizon telescope results. i. the shadow of the supermassive black hole," Astrophys. J., Lett. **875**(1), L1 (2019).

17. W. Larson and B. E. Saleh, "Resurgence of Rayleigh's curse in the presence of partial coherence," Optica **5**(11), 1382–1389 (2018).

18. M. Tsang and R. Nair, "Resurgence of Rayleigh's curse in the presence of partial coherence: comment," Optica **6**(4), 400–401 (2019).

19. W. Larson and B. E. Saleh, "Resurgence of Rayleigh's curse in the presence of partial coherence: reply," Optica **6**(4), 402–403 (2019).

20. K. K. Lee and A. Ashok, "Surpassing Rayleigh limit: Fisher information analysis of partially coherent source (s)," in *Optics and Photonics for Information Processing XIII*, vol. 11136 (International Society for Optics and Photonics, 2019), vol. 11136, p. 111360H.

21. Z. Hradil, J. Řeháček, L. Sánchez-Soto, and B.-G. Englert, "Quantum fisher information with coherence," Optica **6**(11), 1437–1440 (2019).

22. K. Liang, S. A. Wadood, and A. Vamivakas, "Coherence effects on estimating two-point separation," Optica **8**(2), 243–248 (2021).

23. J. Hassett, T. Malhorta, M. Alonso, R. Boyd, S. H. Rafsanjani, and A. Vamivakas, "Sub-rayleigh limit localization with a spatial mode analyzer," in "Frontiers in Optics," (Optical Society of America, 2018), pp. JW4A–124.

24. E. Wolf, "New spectral representation of random sources and of the partially coherent fields that they generate," Opt. Commun. **38**(1), 3–6 (1981).

25. M. Tsang, R. Nair, and X.-M. Lu, "Quantum information for semiclassical optics," in *Quantum and Nonlinear Optics IV*, vol. 10029 (International Society for Optics and Photonics, 2016), p. 1002903.

26. R. Horstmeyer, R. Heintzmann, G. Popescu, L. Waller, and C. Yang, "Standardizing the resolution claims for coherent microscopy," Nat. Photonics **10**(2), 68–71 (2016).

27. Z. Hradil, D. Koutnỳ, and J. Řeháček, "Exploring the ultimate limits: super-resolution enhanced by partial coherence," Opt. Lett. **46**(7), 1728–1731 (2021).

28. J. de Almeida, J. Kołodyński, C. Hirche, M. Lewenstein, and M. Skotiniotis, "Discrimination and estimation of incoherent sources under misalignment," Phys. Rev. A **103**(2), 022406 (2021).

29. M. Gessner, C. Fabre, and N. Treps, "Superresolution limits from measurement crosstalk," Phys. Rev. Lett. **125**(10), 100501 (2020).

30. P. Boucher, C. Fabre, G. Labroille, and N. Treps, "Spatial optical mode demultiplexing as a practical tool for optimal transverse distance estimation," Optica **7**(11), 1621–1626 (2020).

31. M. R. Grace, Z. Dutton, A. Ashok, and S. Guha, "Approaching quantum-limited imaging resolution without prior knowledge of the object location," J. Opt. Soc. Am. A **37**(8), 1288–1299 (2020).

32. B. Rodenburg, M. Mirhosseini, O. S. Magaña-Loaiza, and R. W. Boyd, "Experimental generation of an optical field with arbitrary spatial coherence properties," J. Opt. Soc. Am. B **31**(6), A51–A55 (2014).

33. X. Chen, J. Li, S. M. H. Rafsanjani, and O. Korotkova, "Synthesis of Im-Bessel correlated beams via coherent modes," Opt. Lett. **43**(15), 3590–3593 (2018).

34. V. Arrizón, U. Ruiz, R. Carrada, and L. A. González, "Pixelated phase computer holograms for the accurate encoding of scalar complex fields," J. Opt. Soc. Am. A **24**(11), 3500–3507 (2007).

35. T. Malhotra, W. E. Farriss, J. Hassett, A. F. Abouraddy, J. R. Fienup, and A. N. Vamivakas, "Interferometric spatial mode analyzer with a bucket detector," Opt. Express **26**(7), 8719–8728 (2018).

36. Recall that BSPADE uses only two sets of modes, and the odd modes contain most of the FI for the sub-Rayleigh regime. Thus the BSPADE CRB is very close to the quantum CRB for $\delta < \sigma$, and both are exactly equal in the limit $\delta \to 0$.

37. G. Sorelli, M. Gessner, M. Walschaers, and N. Treps, "Optimal observables for practical super-resolution imaging," arXiv preprint arXiv:2102.05611 (2021).

38. M. Tsang, "Subdiffraction incoherent optical imaging via spatial-mode demultiplexing," New J. Phys. **19**(2), 023054 (2017).

39. M. Tsang, "Quantum limit to subdiffraction incoherent optical imaging," Phys. Rev. A **99**(1), 012305 (2019).

40. M. Tsang, "Semiparametric bounds for subdiffraction incoherent optical imaging: a parametric-submodel approach," arXiv preprint arXiv:2010.03518 (2020).

Optics EXPRESS

Experimental demonstration of superresolution of partially coherent light sources using parity sorting: supplement

S. A. Wadood,[1,2] **Kevin Liang,**[1,2] **Yiyu Zhou,**[1,2] **Jing Yang,**[2,3] **M. A. Alonso,**[1,2,4] **X.-F. Qian,**[5] **T. Malhotra,**[2,3,6] **S. M. Hashemi Rafsanjani,**[7] **Andrew N. Jordan,**[2,3,8] **Robert W. Boyd,**[1,2,3,9] **and A. Nick Vamivakas**[1,2,3,10,*]

[1]*The Institute of Optics, University of Rochester, Rochester, New York 14627, USA*

[2]*Center for Coherence and Quantum Optics, University of Rochester, Rochester, New York 14627, USA*

[3]*Department of Physics and Astronomy, University of Rochester, Rochester, New York 14627, USA*

[4]*Aix Marseille Univ, CNRS, Centrale Marseille, Institut Fresnel, UMR 7249, 13397 Marseille Cedex 20, France*

[5]*Department of Physics and Center for Quantum Science and Engineering, Stevens Institute of Technology, Hoboken, NJ 07030, USA*

[6]*Currently with Facebook Reality Labs, Redmond, WA, USA*

[7]*Department of Physics, University of Miami, Coral Gables, Florida 33146, USA*

[8]*Institute for Quantum Studies, Chapman University, Orange, California 92866, USA*

[9]*Department of Physics, University of Ottawa, Ottawa, Ontario K1N 6N5, Canada*

[10]*Materials Science, University of Rochester, Rochester, NY 14627, USA*

*nick.vamivakas@rochester.edu

Supplementary Material : Experimental demonstration of superresolution of partially coherent light sources using parity sorting

S. A. Wadood,[1,2]**, Kevin Liang,**[1,2] **Yiyu Zhou,**[1,2] **Jing Yang,**[2,3] **M. A. Alonso,**[1,2,4] **X.-F. Qian,**[5] **T. Malhotra,**[2,3†] **S. M. Hashemi Rafsanjani,**[6] **Andrew N. Jordan,**[2,3,7] **Robert W. Boyd,**[1,2,3,8] **and A. Nick Vamivakas**[1,2,3,9]**.**

[1]*The Institute of Optics, University of Rochester, Rochester, New York 14627, USA*

[2]*Center for Coherence and Quantum Optics, University of Rochester, Rochester, New York 14627, USA*

[3]*Department of Physics and Astronomy, University of Rochester, Rochester, New York 14627, USA*

[4]*Aix Marseille Univ, CNRS, Centrale Marseille, Institut Fresnel, UMR 7249, 13397 Marseille Cedex 20, France*

[5]*Department of Physics and Center for Quantum Science and Engineering, Stevens Institute of Technology, Hoboken, NJ 07030, USA*

[6]*Department of Physics, University of Miami, Coral Gables, Florida 33146, USA*

[7]*Institute for Quantum Studies, Chapman University, Orange, California 92866, USA*

[8]*Department of Physics, University of Ottawa, Ottawa, Ontario K1N 6N5, Canada*

[9]*Materials Science, University of Rochester, Rochester, NY 14627, USA*

[†]*Currently with Facebook Reality Labs, Redmond, WA, USA*

[*]*Corresponding author: nick.vamivakas@rochester.edu*

Abstract: This document provides supplementary information to 'Experimental demonstration of superresolution of partially coherent light sources using parity sorting' by Wadood *et al.*

S1. Derivation of Eqs. (2-3) of the main text

In this section, we derive Eqs. (2-3) of the main text. In the object plane, consider two monochromatic point source emitters separated by δ, each emitting N_0 photons. The degree of (spatial) coherence between the two sources is γ. In the Coherent Mode Decomposition (CMD), the cross-spectral density (CSD) $W_O(x_1, x_2)$ at the object plane is given by

$$W_O(x_1, x_2) = N_0 \sum_{k=1}^{2} p_k \phi_k^*(x_1) \phi_k(x_2), \qquad (S1)$$

where $p_1 + p_2 = 1$, $p_1 - p_2 = \gamma$, $p_{1,2} = (1 \pm \gamma)/2$, and $\phi_k(x) = f_+(x) - e^{ik\pi} f_-(x)$ are the symmetric (k=1) and antisymmetric (k=2) coherent modes. In the object plane, $f_\pm(x) = \eta(x \pm \delta/2)$, where $\eta(x)$ are localized functions describing the point sources, and can be considered as regularized delta functions with a unit intensity integral, such that each source individually emits N_0 photons. Equation (S1) shows that total object plane photon number $\int dx W_O(x, x) = 2N_0(p_1 + p_2) = 2N_0$ is given by sum of intensities of the symmetric and antisymmetric modes. At the object plane, these coherent modes are orthogonal. In fact unitary propagation of the field preserves their orthogonal nature. However, the modes do not remain orthogonal after passing through the aperture of the imaging system, which is the fundamental cause of the loss of resolution.

Recall that the finite width of the point spread function (PSF) arises due to the nonunitary nature of the imaging system; the aperture behaves as a low pass filter, blocking photons of spatial frequencies higher than those determined by the system's numerical aperture [1]. Consider the canonical $4f$ imaging system with a Gaussian aperture of width σ_{ap} at the Fourier plane. For

simplicity, consider the lenses to be of infinite extent. Since the propagation up to the aperture is unitary, the number of photons hitting the aperture is $2N_0$. There are $2N_0p_1 = N_0(1 + \gamma)$ photons in the symmetric and $2N_0p_2 = N_0(1 - \gamma)$ photons in the antisymmetric mode hitting the aperture. At the aperture/Fourier plane, these modes behave like a cosine and sine, each with spatial frequency $g = k\delta/2f$, where k is the wavenumber and f is the focal length [1]. For a large δ such that $\sigma_{ap}g \gg 1$, the aperture samples many periods of the coherent modes. The aperture transmission is then a radiometric factor equal to the ratio σ_{ap}/σ_b, where σ_b is the beam width at the aperture. This factor is same for both the coherent modes in the limit $\sigma_{ap}g \gg 1$. As δ becomes smaller such that $\sigma_{ap}g \ll 1$, the aperture samples less than a fringe period of the coherent modes. This is the sub-Rayleigh regime of our interest. For the cosine modes, the aperture samples the peak of the fringe. For the sine modes, the aperture samples the fringe minimum. The smaller δ gets, the transmission for the sine mode decreases, and the transmission for the cosine mode increases. The transmitted photons $I_{1,2}$ for each mode are then given by

$$N_1 = 2N_0p_1 \int dx \left(\frac{1}{8\pi\sigma_b^2}\right)^{1/2} 4\cos^2(gx)\, e^{-\frac{x^2}{2\sigma_b^2}}\, e^{-\frac{x^2}{2\sigma_{ap}^2}} = 2N_0p_1 \frac{\sigma_{ap}}{\sigma_b}\left(1 + e^{-2g^2\sigma_{ap}^2}\right), \quad (S2)$$

$$N_2 = 2N_0p_2 \int dx \left(\frac{1}{8\pi\sigma_b^2}\right)^{1/2} 4\sin^2(gx)\, e^{-\frac{x^2}{2\sigma_b^2}}\, e^{-\frac{x^2}{2\sigma_{ap}^2}} = 2N_0p_2 \frac{\sigma_{ap}}{\sigma_b}\left(1 - e^{-2g^2\sigma_{ap}^2}\right). \quad (S3)$$

In deriving Eqs. (S2, S3), we have assumed the beam at the aperture is a cosine or sine times a broad Gaussian of width σ_b such that $\sigma_b \gg \sigma_{ap}$. Using $p_1 + p_2 = 1$, we find the total photons *transmitted* by the aperture is given by

$$N_t = N_1 + N_2 = 2N_0 \frac{\sigma_{ap}}{\sigma_b}\left(1 + \gamma e^{-2g^2\sigma_{ap}^2}\right). \quad (S4)$$

Eq. (S4) does not contradict energy conservation. The transmitted photon number $I_1 + I_2$ is not a strictly conserved quantity since it is the photon number in a local (Gaussian-apodized) portion of a fringe pattern. In essence, Eq. (S4) simply shows that the aperture transmission depends on the spatial coherence among two partially coherent emitters.

The propagation from the aperture to the image plane is also unitary, and hence Eqs. (S2-S4) also give the number of symmetric, antisymmetric, and total image plane photons. At the image plane, the Gaussian PSF's width σ is related to σ_{ap} by $k^2\sigma_{ap}^2/f^2 = 1/4\sigma^2$. We then have, using $g = k\delta/2f$, $\exp[-2g^2\sigma_{ap}^2] = \exp[-\delta^2/8\sigma^2] = d$, where d is the overlap integral of the Gaussian PSFs. The overlap is generated due to the nonunitary nature of the aperture, as is evident from our analysis. Moreover, the image plane CSD given in Eq. (1) of the main text is found by substituting $f \pm (x) = \frac{e^{-(x\pm\delta/2)^2/4\sigma^2}}{(2\pi\sigma^2)^{1/4}}$, and $\kappa = \sigma_{ap}/\sigma_b$ in Eq. (S1). Formally, the image and object plane CSDs can be connected by propagating the coherent modes through the nonunitary imaging system. Finally, by substituting $\kappa = \sigma_{ap}/\sigma_b$ and using $p_{1,2} = (1 \pm \gamma)/2$, Eqs. (S2-S4) reduce to Eqs. (2,3) of the main text.

S2. Derivation of Eqs. (4,5) of the main text

Assuming Poisson statistics and using Eqs. (S2, S3), we derive the FI matrix as

$$
J = \sum_{i=1,2}
\begin{bmatrix}
\frac{1}{N_i}\left(\frac{\partial N_i}{\partial \delta}\right)^2 & \frac{1}{N_i}\left(\frac{\partial N_i}{\partial \delta}\right)\left(\frac{\partial N_i}{\partial N_0}\right) \\
\frac{1}{N_i}\left(\frac{\partial N_i}{\partial N_0}\right)\left(\frac{\partial N_i}{\partial \delta}\right) & \frac{1}{N_i}\left(\frac{\partial N_i}{\partial N_0}\right)^2
\end{bmatrix},
$$

$$
=
\begin{bmatrix}
N_0 \frac{\delta^2 d^2}{8\sigma^4}\left(\frac{1-\gamma d}{1-d^2}\right) & -\frac{\gamma \delta d}{2\sigma^2} \\
-\frac{\gamma \delta d}{2\sigma^2} & \frac{2}{N_0}(1 + \gamma d)
\end{bmatrix}.
\tag{S5}
$$

If only δ is unknown, the FI normalized by the object plane photon number $2N_0$ is described by $J(1,1)/2N_0$, which is equivalent to Eq. (4) of the main text and is plotted in Fig. (1a) of the main text.

If both δ and N_0 are unknown, the FI for estimating δ is found by $(C(1,1))^{-1}$, where $C = J^{-1}$, and $C(1,1)$ gives the multiparameter CRB. The matrix C is given as

$$
C = \frac{1}{\frac{\delta^2 d^2}{4\sigma^4}\left(\frac{1-\gamma^2}{1-d^2}\right)}
\begin{bmatrix}
\frac{2}{N_0}(1 + \gamma d) & \frac{\gamma \delta d}{2\sigma^2} \\
\frac{\gamma \delta d}{2\sigma^2} & N_0 \frac{\delta^2 d^2}{8\sigma^4}\left(\frac{1-\gamma d}{1-d^2}\right)
\end{bmatrix}.
\tag{S6}
$$

The quantity $(C(1,1))^{-1}/2N_0$ is given by Eq. (5) of the main text and plotted in Fig. (1b) of the main text.

S3. Offline Coherence Synthesis and Modal Weights vs. γ

In this section, we describe the offline coherence synthesis and measurements of the normalized image plane modal weights $m_{1,2} = N_{1,2}/N_t$, where $N_t, N_{1,2}$ are given by Eqs. (2,3) of the main text.

Since we are working in the image plane model, we do not know N_0 as explained in the Theory section of the main text. For this section, we therefore denote the symmetric and antisymmetric experimental photon numbers as $N_{sym,asym}$ instead of $N_{1,2}$ as used in Eq. (3) of the manuscript. For a fixed δ, we prepare an antisymmetric mode and record its photon number N_{asym} at the output of the parity sorter. N_{asym} can be arbitrary but is dictated by experimental limitations such as phase noise of the interferometer, electronic noise and dynamic range of the detector etc. We then prepare a symmetric mode for the given δ, and record its flux at the output of the parity sorter over a wide range of input powers. For a particular γ and δ, the corresponding photon number N_{sym} of the symmetric mode is given as $N_{sym} = KN_{asym}$, where $K = (1+\gamma)(1+d)/(1-\gamma)(1-d)$. The modal weights are normalized by $N_t = N_{sym} + N_{asym}$ such that $m_{1,2} = N_{sym,asym}/(N_t)$. We then post-select values for the desired γ. For example, assume $\delta = 0.5\sigma$, and 1 photon in the antisymmetric mode, i.e., $N_{asym} = 1$. For $N_{sym} = \{0, 10, 64, 100\}$ photons in the symmetric mode, the γ would correspond to $\{-1, -0.72, 0, 0.2\}$ respectively. Note that the post-selected N_{sym} and N_{asym} are random variables which include both the quantum shot noise and the classical electronic and optical noise of the system. The post-selection is only applied to the 'mean' values of N_{asym} and N_{sym} satisfying $\langle N_{sym}\rangle = K\langle N_{asym}\rangle$, as explained in the Image processing section. We emphasize that experimentally, in the image plane model and offline coherence synthesis afforded by the CMD, N_t is defined as equal to $N_{sym} + N_{asym}$ (the total photons in the interferometer) and does not depend on δ or γ as in the object plane model of Eq. (2) of the main text.

Figure (S1) shows the measured modal weights for different γ values. The solid red and blue lines in Fig. (S1a-c) are theoretically expected plots of even and odd modal weights respectively. The dashed lines are the theoretically expected plots incorporating effects of cross-talk. The
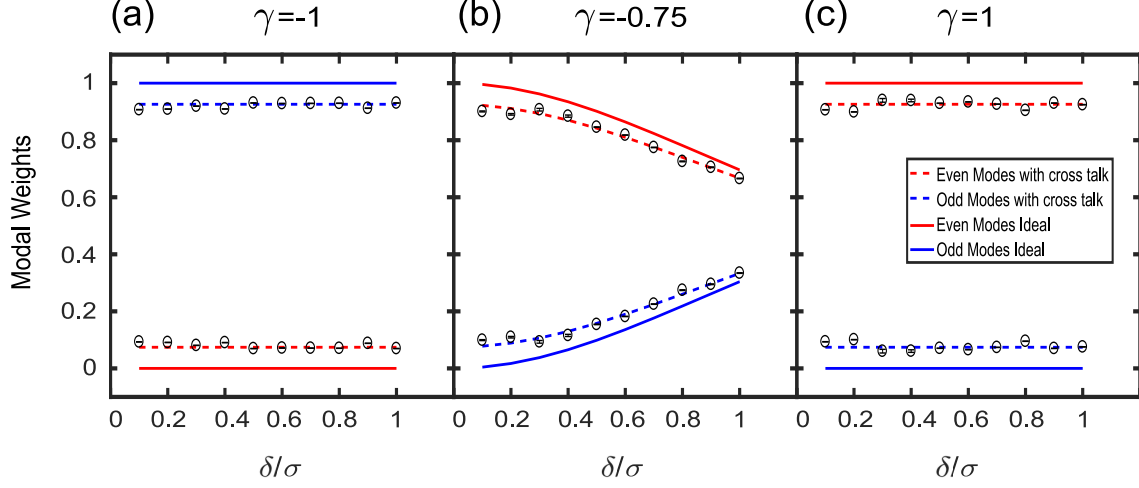
Fig. S1. Measured modal weights for the parity sorter. a-c: Modal weights for $\gamma = -1, 1, -0.75$. Blue and red color indicates the odd and even modal weights respectively. Solid lines indicate the theoretically expected modal weights with zero cross-talk. The dashed lines indicate the expected modal weights for 8% cross-talk. The circles indicate the measured values. All the modal weights are normalized by N_t, the total number of photons in the interferometer. Each point on the graphs represents a mean of 10 measurements, while the error bars are too small to be noticed on the graph. Note that for $|\gamma| = 1$, the modal weights are constant versus δ.

circles indicate the mean values of data recorded for 10 measurements. For $|\gamma| = 1$, all the optical power is directed into a single port; $P_1 = 1$ (solid red line) and $P_2 = 0$ (solid blue line) for $\gamma = 1$. Similarly $P_1 = 0$ and $P_2 = 1$ for $\gamma = -1$. If the optical power in either port does not change as a function of δ, which is the parameter to be estimated, one would expect no information to be gained by parity sorting. The error bars on all figures are too small to be visible on the graph. Finally, Fig. (S1 b) shows the modal weights measured for $\gamma = -0.75$. The modal weights change rapidly with δ, and therefore one would expect a higher FI for $\gamma = -0.75$ than for $\gamma = 1, -1$.

When processing the measured optical powers for the maximum likelihood estimation (MLE), we have subtracted any cross-talk, which was 8% on average, between the two ports. The cross-talk could be attributed to intensity mismatch of the two beams, finite coherence time, and fluctuations of path length and polarization in the two arms. This background subtraction is allowed because we are generating coherence offline by adding post-selected intensities, and only one of the coherent modes is present at a given time. Better alignment of the system can reduce the cross-talk. However, this experimental complexity is irrelevant to the analysis of partial coherence and thus is avoided in our proof-of-principle experiment by using offline coherence generation. Figure (S2) shows the cross-talk subtracted modal weights measured for $\gamma = 0, \pm, 0.25, \pm 0.5$. Note that for a given δ, the power in the symmetric (antisymmetric) mode increases (decreases) as γ becomes more positive.

S4. Experimental Details

S4.1. Mode Intensity vs. δ

In our superresolution experiment we directly prepare the image plane CSD, represented by Eq. (1) of the main text, through the SLM and subsequent offline addition of modes. Specifically, this technique allows us to avoid the more complicated procedure of preparing two actual emitters with varying γ and δ, with a CSD given by Eq. (S1), and a physical Gaussian aperture whose
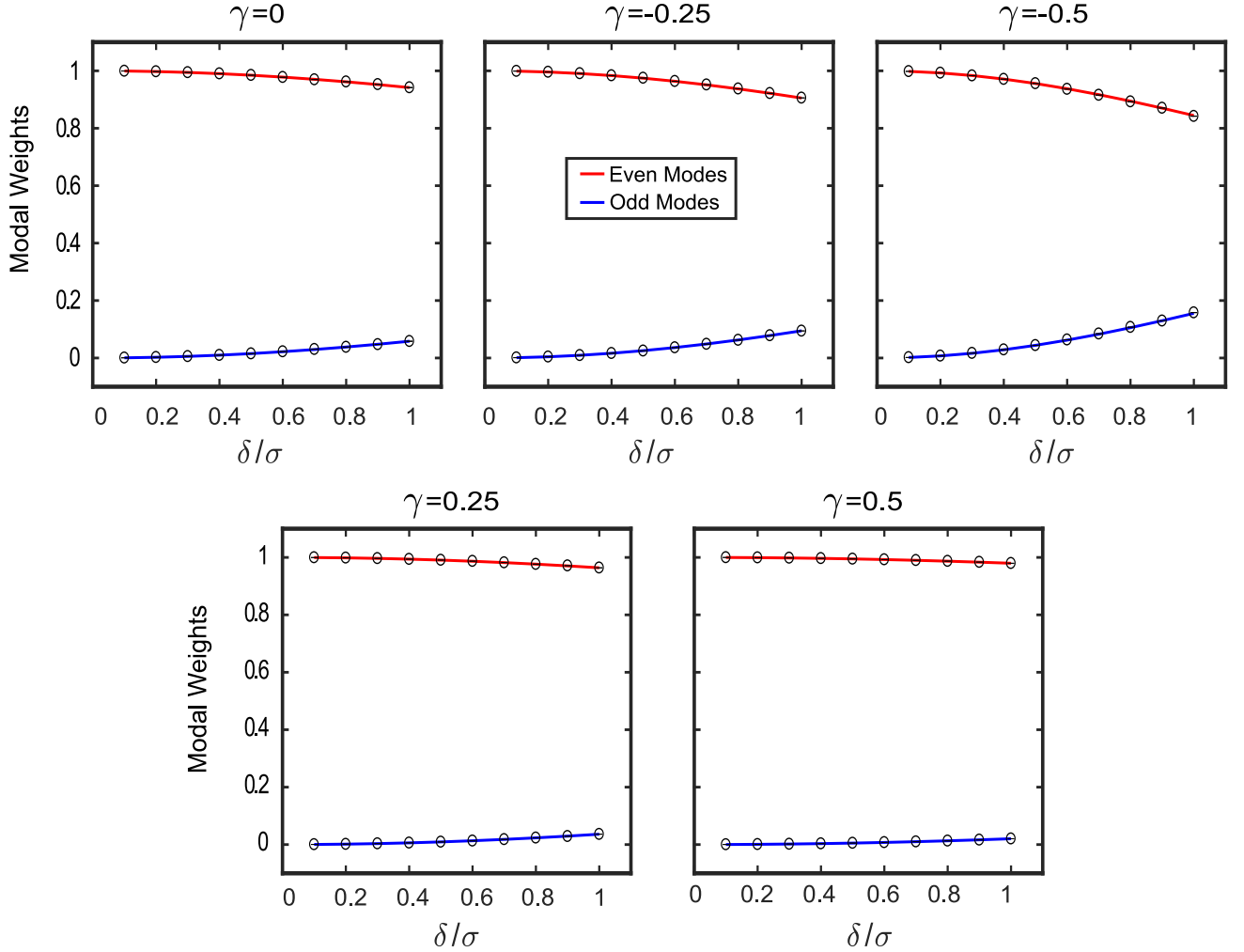
Fig. S2. Measured and expected modal weights for the parity sorter for $\gamma = 0, \pm0.25, \pm0.5$. Blue and red solid lines respectively indicate the theoretically expected modal weights for antisymmetric and symmetric mode. The circles indicate the measured modal weights. Each point on the graphs represents a mean of 10 measurements, while the error bars are too small to be noticed on the graph. Note that cross-talk has been subtracted for this data.

transmission varies according to Eq. (S2-S4). To this end, the power in the coherent modes does not depend on δ. This is because the SLM is fundamentally a phase grating whose first diffraction order contains the desired coherent mode. Ideally, the efficiency of the grating is independent of δ, except for the zero-photon case of $\gamma = -1$ and $\delta = 0$ in which case no grating phase is implemented. As long as the SLM pixel pitch and phase modulation range are not the bottleneck for a given phase grating, the grating efficiency and hence the power in a mode will not change with δ. Figure (S3) shows the power in the symmetric and antisymmetric modes measured for a fixed input power incident on the SLM. We see that the mode power is independent of δ. The grating efficiency for the symmetric mode is actually lower than the antisymmetric mode, which causes the lower power in the symmetric mode. We can control the power going to the interferometer with polarization optics, and can control the powers of the mode *after* the SLM.
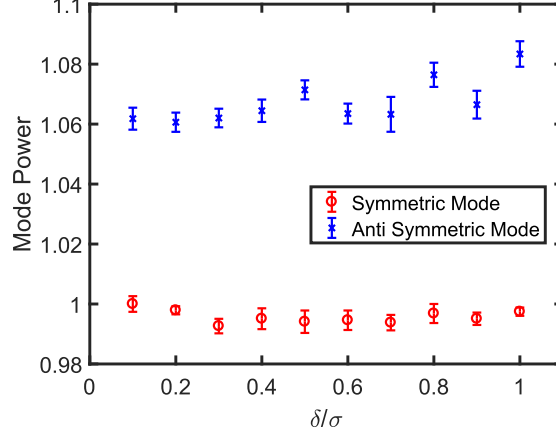
Fig. S3. Power in the Coherent modes versus δ for fixed input laser power impinging on the SLM. The power has been normalized to the power in the Symmetric mode for $\delta = 0.1\sigma$. Note that the power in the antisymmetric mode is consistently higher because of the higher diffraction efficiency of the SLM phase grating required to generate the antisymmetric mode. Ten images were taken for each data point.

S4.2. Image Processing

The basic idea of coherent mode decomposition (CMD) is to add the symmetric and antisymmetric modes on an intensity basis. For a specific δ and γ, the relative intensity of the symmetric and antisymmetric mode is $m_1/m_2 = K = (1 + \gamma)(1 + d)/(1 - \gamma)(1 - d)$ as evident from Eq. (3) in the main text. For example, if $\gamma = 0$ and $d = \exp(-\delta^2/8\sigma^2) = 0.5$ (which implies that $(\delta/\sigma)^2 = -8\ln[0.5]$), then $m_1/m_2 = 3$. To 'prepare' the $\gamma = 0$ intensity offline for this δ, one then needs to have a symmetric mode with thrice the power of the antisymmetric mode. As will be explained below, we post-select the required powers for each coherent mode from an array of recorded powers. These post-selected powers are then used to obtain the ML estimate $\hat{\delta}$. This process is repeated 100 times and the variance $\text{Var}[\hat{\delta}]$ is then compared with the CRB.

We measure $\text{Var}[\hat{\delta}]$ for $\gamma = 0$ and $\gamma = -0.75$. For these γ values and $\delta/\sigma < 1$, the power in the symmetric mode is always larger than the power in the antisymmetric modes, as is evident from Figs. (S1,S2). Therefore, a large dynammic range is required to accurately measure these modal weights. To increase the dynamic range of our measured powers, we use the fact that our problem is 1D (x dimension), while the coherent mode is 2D; the coherent modes are a symmetric zeroth order Gaussian in y. The integrated power in each row of the coherent mode then corresponds to an independent parity sorting measurement. N rows in the mode then correspond to N bucket detectors performing parity sorting measurements. Figure (S4) shows an image of the coherent modes and the marginals for $\delta = 0.4\sigma$. Specifically, each point on the Y marginal is used as an independent realization of a parity sorting measurement. This is allowed because we are using an approximately single-mode laser source, for which the pixels on the CCD are uncorrelated in intensity [2]. It is from these Y marginals of the symmetric and antisymmetric modes that we choose the photon numbers $N_{sym,asym}$ such that $N_{sym} = KN_{asym}$.

To saturate the Cramer–Rao bound (CRB), the system should be shot-noise limited. This means that the photon numbers used from the Y marginals should have Poisson statistics. We use a low noise Gigajot CCD with a dark current of less than 0.5 $e - /s$/pixel at room temperature [3]. The photoelectron statistics of each arm of the interferometer are shot noise limited, as can be found by blocking the other arm. We show the noise statistics of the interferometer output in Fig. (S5). For
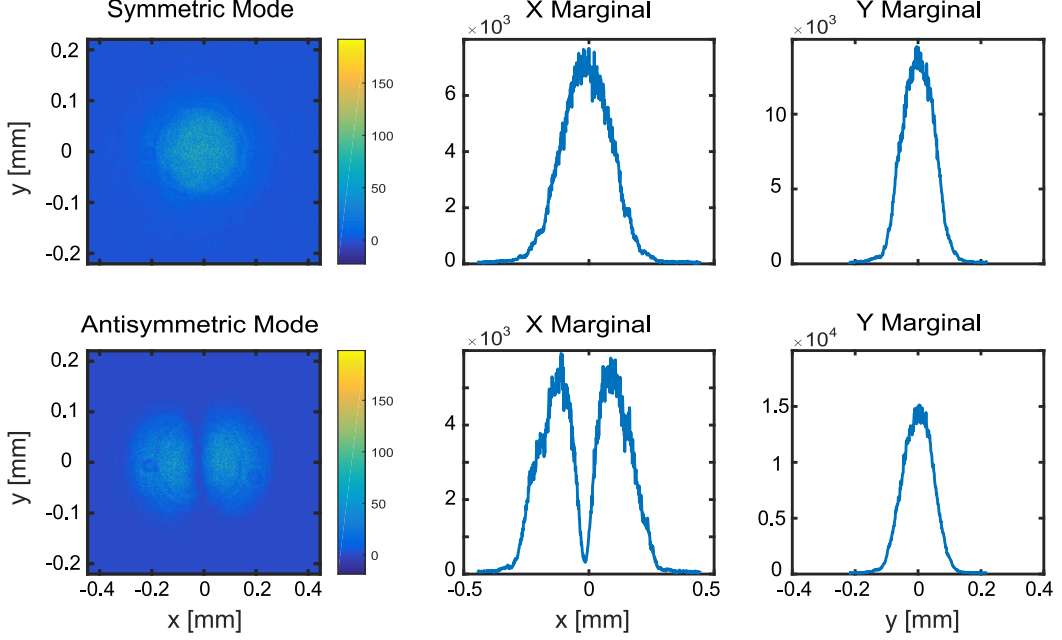
Fig. S4. Sample Image of Coherent Modes and their marginals for $\delta = 0.4\sigma$. Each pixel value on the Y marginal is counted as a bucket detector output in the parity sorter. The colorbar on the mode images and the y-axis on the marginals represent the detected photoelectron number.

every pixel on the Y marginal, we have three numbers: (i) the mean intensity $\langle I(y) \rangle$ (circles and solid blue line), where $I(y) = \int dx |\phi(x,y)|^2$ is the integrated intensity across x and the ensemble average is taken across the 100 acquired images. (ii) The variance $\langle \Delta I^2(y) \rangle = \langle I^2(y) \rangle - \langle I(y) \rangle^2$ (solid orange line), and (iii) the noise metric $M(y) = (\langle \Delta I^2(y) \rangle - \langle I(y) \rangle)/\langle I(y) \rangle$ (cross and solid purple line). $M \approx 0$ corresponds to shot noise statistics, while any classical (electronic or optical) fluctuations will increase the value of M. In Fig. (S5), the reference arm statistics shows that the centre portion of the Y marginal Gaussian is close to being shot noise limited because of the high intensity, as opposed to the tails of the Gaussian. In contrast, the interference images, for which both arms are unblocked, have high M values in the centre of the Gaussian. Note that the classical noise is more pronounced in the antisymmetric mode compared to the symmetric mode.

The major noise source in our interferometer is phase noise due to path length fluctuations in the interferometer. Moreover, the phase noise fluctuations do not affect the coherent modes globally. This is due to the mode inhomogeneities introduced due to phase jumps in the SLM arm of the interferometer [4] that implements the $2f$ system. The peaks in the noise of the interference images in Fig. (S5) are due to the mode inhomogeneities caused mainly due to phase rings of the SLM coupled with the path length fluctuations. However, there is a significant number of rows that are are relatively less affected by phase fluctuations such that $M(y) < 1$. These are the rows we use in the ML estimator. We sort the rows in ascending order according to the metric $M(y)$, and use these sorted rows in the CMD; rows with the lowest absolute $M(y)$ value is picked first for CMD. Note that $M(y) < 0$ is possible because of the finite size of our ensemble of 100 images, and we therefore sort based on $|M(y)|$ rather than $M(y)$. A consequence of our CMD algorithm is that data for a higher γ will have a higher photon number. This is because for a higher γ on the real line, the ratio m_1/m_2 increases as $1/(1-\gamma)$, and hence we require more rows of the symmetric mode to generate the required coherent mode power. Another effect of this
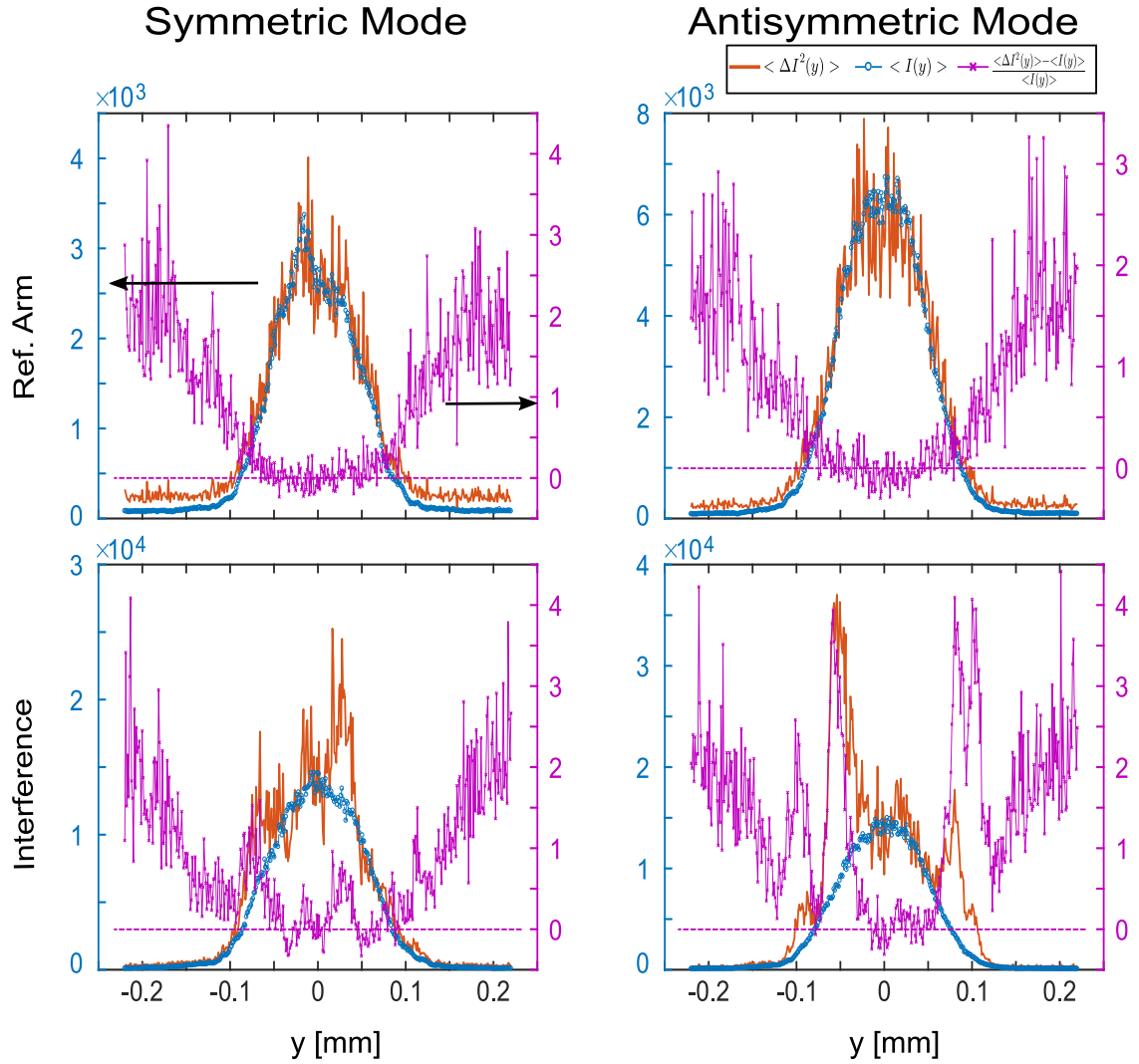
Fig. S5. Noise statistics of the parity sorter. All figures show the statistics of the Y marginal. Top row shows the statistics of the reference arm, with the $2f$ imaging SLM arm blocked. Bottom row shows the statistics of the interference images, with both arms unblocked. Solid blue lines and circles represent the mean value $\langle I(y) \rangle$ over 100 images (blue y-axis on left). Solid orange line represents the variance $\langle \Delta I^2(y) \rangle$. Solid purple line and crosses represent the noise metric $M(y)$ (purple y-axis on right). The dashed purple line represents the shot noise limit $M = 0$. Note that the two reference and interference images were taken separately with different laser powers, so the reference image power is not exactly half that of the interference image power. The text discusses details of the figure.
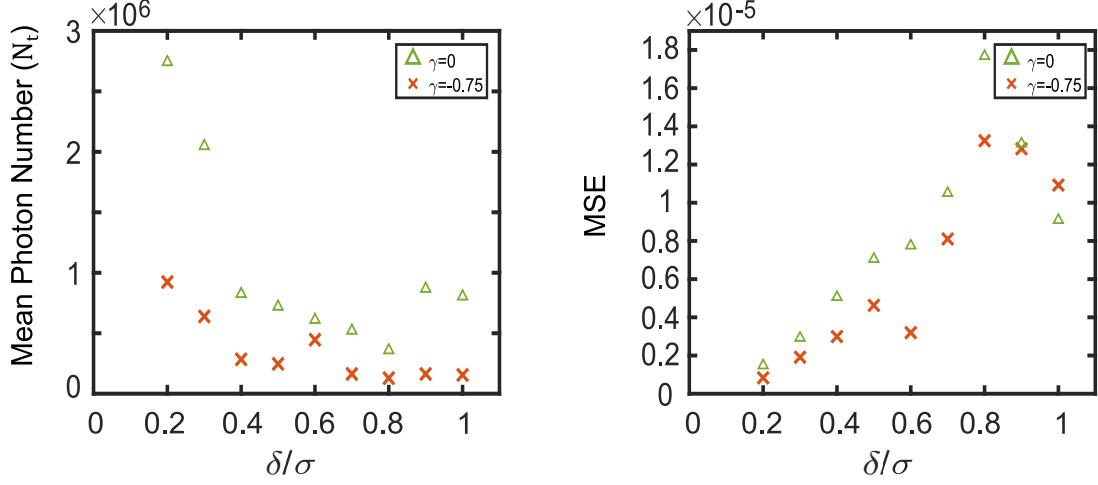
Fig. S6. Left: Mean total image plane photon number N_t per iteration used in estimation of δ. Note that the photon number for $\gamma = 0$ (green triangles) is consistently higher than the photon number for $\gamma = -0.75$. Right: The MSE for $\gamma = 0, -0.75$. The MSE for $\gamma = -0.75$ is less than the MSE for the $\gamma = 0$ case for all but the $\delta = 0.9\sigma$ case.

algorithm is that data for a higher γ will have higher (classical) noise, since more rows are added. The difference in the noise due to the different number of rows is observed to be not significant, however, in our experiment. One way to mitigate this noise difference is to take more images and add them to get a set of 100 images. This will decrease phase fluctuations due to averaging. For $\delta = 0.2 - 0.5$, we took $[500 - 200]$ images and added them together to prepare 100 images each for processing. In Fig. (3) of the manuscript, we compare $\gamma = 0$ and $\gamma = -0.75$, for which the number of rows do not differ significantly and hence the phase noise is approximately the same for both γ cases.

S4.3. Photon number in Fig. (3) of Main text

Figure (3b) of the main text compares the product of the mean squared error (MSE/$4\sigma^2$) and the mean total image plane photon number (N_t) used for each iteration in the 100 estimates. This was done because the CRB lowerbounds the product $N_t \text{Var}[\hat{\delta}]$ and not just $\text{Var}[\hat{\delta}]$. It is still instructive to look at the actual photon number and the mean squared error separately. As explained in the Image Processing section, the mean photon number is not the same for $\gamma = 0$ and $\gamma = -0.75$. In Fig. (S6) we show the actual values of the photon number and the mean squared error, i.e., $\text{Var}[\hat{\delta}]$ for both $\gamma = 0, -0.75$. Note that the photon number for $\gamma = 0$ is consistently *higher* than the photon number for $\gamma = -0.75$. Despite that, because the FI for $\gamma = -0.75$ is higher than the FI for $\gamma = 0$ case, the variance for partially anticorrelated case is *lower* than the variance for the incoherent case for all but the $\delta = 0.9\sigma$ case. Had the photon number in the $\gamma = -0.75$ case been increased to match the $\gamma = 0$ photon number, the variance in the $\gamma = -0.75$ case would have dropped even further. This shows unambiguously that for the same number of photons, partial anticorrelation among the sources leads to a lower variance than the incoherent scenario.

References

1. J. W. Goodman, *Introduction to Fourier Optics* (Roberts and Company Publishers, 2005).
2. L. Mandel and E. Wolf, *Optical Coherence and Quantum Optics* (Cambridge University Press, 1995).
3. J. Ma, S. Masoodian, D. A. Starkey, and E. R. Fossum, "Photon-number-resolving megapixel image sensor at room temperature without avalanche gain," Optica **4**, 1474–1481 (2017).
4. T. Malhotra, W. E. Farriss, J. Hassett, A. F. Abouraddy, J. R. Fienup, and A. N. Vamivakas, "Interferometric spatial mode analyzer with a bucket detector," Optics express **26**, 8719–8728 (2018).